Journal of Electroanalytical Chemistry 662 (2011) 157–168

Contents lists available at ScienceDirect

Journal of Electroanalytical Chemistry

journal homepage: www.elsevier.com/locate/jelechem

Mass transport effects in CO adsorption and continuous CO electrooxidation over regular arrays of Pt nanostructures on planar glassy carbon supports

H. Schwechten [a], M. Heinen [a], Y.E. Seidel [a], Z. Jusys [a], B. Wickman [b], B. Kasemo [b], R.J. Behm [a,*]

[a] Institute of Surface Chemistry and Catalysis, Ulm University, D-89069 Ulm, Germany
[b] Dept. of Applied Physics, Chalmers University of Technology, S-41296 Göteborg, Sweden

ARTICLE INFO

Article history:
Available online 12 June 2011

Keywords:
Electrocatalysis
CO adsorption
CO electrooxidation
Platinum
Nanostructuring
Transport effects

ABSTRACT

The interplay between mass transport and the kinetics of CO adsorption/CO electrooxidation was studied on nanostructured electrodes, which consist of regular arrays of catalytically active cylindrical Pt nanodisks supported on a planar glassy carbon (GC) substrate, and are fabricated via Hole-mask Colloidal Lithography. CO adsorption and oxidation were measured under controlled transport conditions in a thin-layer flow cell interfaced to a mass spectrometer. The temporal evolution of the relative CO_{ad} coverage, the effective sticking coefficient and the dependence of the adsorption rate on the CO_{ad} coverage were evaluated for CO adsorption at 0.06 V (vs. reversible hydrogen electrode) at systematically varied CO concentrations and Pt nanodisk coverages. Continuous CO oxidation was studied at different electrode potentials under identical mass transport condition. While qualitatively, the characteristics of the adsorption/reaction kinetics do not depend on the transport conditions, the absolute rates of CO adsorption and CO (bulk) oxidation, normalized to the Pt coverage, increase strongly with decreasing Pt coverage on the nanostructured Pt/GC electrodes. This is explained by a gradual transition from one-dimensional planar diffusion (concentration gradients planar to the surface–extended Pt surface) to three-dimensional hemispherical diffusion (nanostructured surfaces).

1. Introduction

In recent years we developed novel, nanostructured model electrodes consisting of arrays of rather regularly arranged Pt nanodisks of homogeneous size supported on smooth glassy carbon (GC) substrates as a tool for systematic studies of transport effects in electrocatalytic reactions [1,2]. These electrodes, which were prepared by Colloidal Lithography techniques [3,4], allowed us to independently vary the size and the density of these nanodisks in a controlled way over a wide range (diameter 50–150 nm, height 20–60 nm, density 0.2–8 $\times$ 10^9 cm^{-2}). Utilizing the possibility that the transport conditions could be varied in a controlled way by changing either the size or density of the nanodisks or the flow rate of the electrolyte, these electrodes were employed for a number of systematic studies performed under well defined reaction and transport conditions, including the O_2 reduction reaction (ORR) [5,6], the oxidation of methanol [7], and the oxidation of formaldehyde [8,9]. The main focus of those studies was to elucidate the influence of transport conditions on the selectivity (product distribution) of these reactions, which were found to sensitively depend on the transport conditions [6].

Similar methods can also be applied to study the effect of transport conditions on the measured kinetics of adsorption and reaction processes. This novel aspect is topic of the present study, where we investigated the (measured) kinetics of CO adsorption and, at higher potentials, of simultaneous CO oxidation on nanostructured Pt/GC electrodes. The interaction of CO with metal surfaces, including its adsorption kinetics, has been a key topic in Surface Science and hence been widely studied over the last half a century, both experimentally and theoretically [10]. Numerous studies were performed also on the metal–CO interaction at the electrified solid–liquid interface [11–15], both from a fundamental interest and, more recently, because of the role of CO in Polymer Electrolyte Fuel Cell technology [16]. The kinetics of CO adsorption and hence of CO adlayer build-up, however, was rarely studied so far [17–20]. Major reason for that is the ill-defined mass transport of dissolved gaseous species to the electrode surface, which can be overcome only by applying hydrodynamic methods that ensure a controlled delivery of reactants to the electrode surface in the liquid phase [21]. The same is valid for the continuous electrochemical oxidation of gaseous species such as CO ('CO bulk oxidation') [18,22–27].

The CO adsorption kinetics under well-defined mass transport conditions can either be monitored via the loss of CO in the electrolyte, e.g., by on-line differential electrochemical mass spectrometry (DEMS) in a thin-layer flow cell [18], or via the build-up of the CO adlayer by *in situ* spectroscopy under continuous flow conditions,

* Corresponding author.
E-mail address: juergen.behm@uni-ulm.de (R.J. Behm).

1572-6657/$ - see front matter © 2011 Elsevier B.V. All rights reserved.
doi:10.1016/j.jelechem.2011.05.021

e.g., by *in situ* FTIR spectroscopy in an attenuated total reflection (ATR) configuration [28,29]. Employing combined ATR-FTIRS/DEMS measurements, the CO adlayer build-up [20,28] and CO bulk oxidation on thin-film Pt electrodes [29] were investigated recently in an electrochemical environment under controlled transport conditions. CO adsorption/oxidation on a polycrystalline Pt microelectrode was studied recently employing time-resolved reflectance spectroscopy for probing the adlayer build-up and the resulting steady-state CO_{ad} coverage upon continuous CO oxidation [30].

In the present study, the interplay between reactant transport and CO adsorption kinetics was investigated by on-line DEMS in a flow cell, using nanostructured Pt/GC samples as working electrodes. The mass transport to the electrode surfaces was varied by changing the CO concentration in the supporting electrolyte (1.0, 0.3 and 0.1 vol.%) and/or the density of the Pt nanodisks (geometric Pt coverage 100%, 28%, 13% and 7%). The experimental situation can be considered as a flux of reactant species to an array of ultra-microelectrodes (UMEs) located in an inert planar surrounding, which is described by a combination of planar diffusion (1D concentration gradients perpendicular to the surface) further away from the electrode surface and an enhanced hemispherical diffusion (3D concentration gradients) to these UMEs close to the surface [31–33]. Quantitative experimental evaluation of the transport characteristics under these conditions, including the transition from planar diffusion over an extended electrode surface to increasing contributions from hemispherical diffusion over the UMEs would be highly interesting and provide detailed information about the (reactant) transport characteristics in the vicinity of the electrode.

In the following, we will, after a brief description of the experimental set-up and procedures, first characterize the morphology and electrochemical properties of these electrodes (Section 3.1), and then present and discuss data on the measured CO adsorption kinetics on nanostructured Pt/GC electrodes and, for comparison, on an extended, polycrystalline Pt (pc-Pt) electrode at different CO concentrations (Section 3.2), and on CO bulk oxidation at different electrode potentials under identical electrolyte flow conditions (Section 3.3). Finally, the kinetic limitations in the latter reaction are quantitatively evaluated.

2. Experimental

2.1. Preparation and physical characterization of the nanostructured electrodes

The nanostructured samples were prepared via Hole-mask Colloidal Lithography (HCL) (for details see Ref. [2]). After (i) an initial oxygen plasma pre-treatment (50 W, 330 mbar, 2 min) of the glassy carbon substrates to remove surface contaminations, (ii) a sacrificial poly(methyl methacrylate) (PMMA) resist layer was deposited by spin coating, followed by, (iii) deposition of masking polystyrene (PS) beads on top of the PMMA layer on the GC substrate, subsequently, (iv) a 20 nm thick, plasma-resistant Au film was evaporated on top of the PMMA layer and the masking PS beads, and then (v) the Au-covered PS beads were removed by tape-stripping, leaving well-defined holes in the Au film where the PS beads had been. This results in the so-called hole-mask, subsequently, (vi) the unprotected, bare PMMA film in the holes of the mask was removed by oxygen plasma etching, and (vii) Pt was evaporated on the PMMA/Au hole-mask-covered GC surface. Finally, the PMMA/Au hole-mask was lifted off in acetone, leaving Pt nanodisks of well-defined size and lateral distribution on the GC substrate.

The morphology of the nanostructured electrodes was characterized by scanning electron microscopy (SEM) using a LEO 1550 (Zeiss) microscope (10 kV accelerating voltage).

2.2. Electrochemical measurements and experimental protocol

The electrochemical measurements were performed in a DEMS system, which consists of two coupled, differentially pumped chambers, a Balzers QMS 422 quadrupole mass spectrometer, and a Pine Instruments potentiostat [18]. Electrochemical and on-line mass spectrometry measurements were performed simultaneously, using a dual thin-layer flow cell with the working electrode in the first thin-layer compartment and a membrane (Scimat®, 60 μm thick, 50% porosity, 0.2 μm pore diameter) inlet system into the mass spectrometer in the second thin-layer compartment.

The electrolyte was continuously purged by the respective gases (Ar, Ar/CO mixtures or CO), its flow was controlled via a valve installed at the outlet of the cell. A saturated calomel electrode (SCE) connected to the outlet of the dual thin-layer flow cell through a Teflon capillary served as the reference electrode. However, all potentials are quoted vs. that of the reversible hydrogen electrode (RHE). The supporting electrolyte (0.5 M H_2SO_4) was prepared using Millipore MilliQ water and sulfuric acid (Merck, suprapur) and de-aerated by high purity Ar gas (MTI Gases, N 6.0). The CO adsorption transients were recorded in base electrolyte purged with dilute CO/Ar mixtures (1.0 vol.%, 0.3 vol.% and 0.1 vol.% CO in Ar, CO 4.7, Ar 6.0, MTI). The CO oxidation experiments were performed in base electrolyte purged with 1.0 vol.% CO in Ar.

Prior to the electrochemical measurements, the nanostructured Pt/GC electrodes were cleaned by rapid cycling at 100 mV s^{-1} in base electrolyte between 0.06 and 1.36 V to remove organic contaminations adsorbed during sample preparation and transport [1].

2.2.1. CO adsorption transients

The electrochemical and mass spectrometric signals (m/z = 44 and m/z = 28) were monitored simultaneously during CO adsorption/oxidation under continuous, controlled electrolyte flow (10 μL s^{-1}). The experimental protocol consisted of: (i) holding the electrode at 0.06 V for 2–3 min to develop a saturated CO adlayer and to achieve stable background signals for the mass spectrometric currents; (ii) stepping the electrode potential to 1.0 V to oxidatively remove the CO_{ad} by continuous oxidation, and finally (iii) stepping the potential back to the adsorption potential of 0.06 V. Depending on the CO concentration and the Pt coverage, the electrode was held at that potential between 3 min and 15 min to ensure that a fully saturated CO adlayer is reached. The uptake of CO (CO adsorption rate) was calculated from the consumption of CO, given by the difference between the mass spectrometric current for m/z = 28 over the CO_{ad} saturated electrode at a given time and the time-dependent m/z = 28 signal [34]. The CO_{ad} coverage at any given time was determined by integrating that difference from the beginning of the adsorption process, directly after the potential step from 1.0 to 0.06 V, to the corresponding adsorption time, divided by the total charge required for saturating the Pt surface with CO_{ad}, which is proportional to the CO_{ad} saturation coverage [18]. To obtain the adsorption rate in terms of monolayer per second (ML s^{-1}), where 1 ML is defined as the saturation coverage obtained under present adsorption conditions, the CO uptake was normalized accordingly. The relative, effective CO sticking coefficient $s_{eff,rel}(\theta)$ at a given CO_{ad} coverage was calculated as the ratio of the CO adsorption rate at that coverage and the highest CO adsorption rate, which was obtained directly after the potential step from 1.0 to 0.06 V.

2.2.2. CO_{ad} monolayer oxidation

Following the CO adsorption transients, CO_{ad} stripping experiments were performed to determine the calibration constant K^* of the present mass spectrometric set-up (for details see Ref. [18]). To ensure complete saturation of the Pt surface, the potential

was kept constant for additional 5 min in electrolyte saturated by 1.0 vol.% CO in Ar after the potential-step to 0.06 V. Subsequently, the cell was rinsed with CO free base electrolyte (~35 min). The adsorbed CO was oxidized in an anodic potential scan up to 1.16 V (scan rate 10 mV s^{-1}), following both the Faradaic current and the mass spectrometric signals for $m/z = 28$ (CO^+) and $m/z = 44$ (CO_2^+).

2.2.3. Continuous CO oxidation

For the CO bulk oxidation measurements under continuous and controlled electrolyte flow (10 μL s^{-1}), we applied the following experimental protocol: After holding the electrode at 0.06 V for ca. 3 min in CO containing electrolyte, the potential was (i) stepped to the respective oxidation potential for 3 min, then (ii) back to 0.06 V for 2 min, followed by (iii) a sequence of potential steps to progressively higher (lower) values (increments of 0.1 V, holding time at each potential 3 min) in the potential range of CO oxidation over the oxygen/oxide covered surface (1.0–1.3 V). This protocol ensures a comparable state of the CO_{ad} covered electrode prior to stepping the potential into the reaction regime. Furthermore, the reaction potential was reached in sequences of increasing and decreasing reaction potentials, respectively, to ensure the reproducibility of the measurements.

3. Results and discussion

3.1. Characterization of the nanostructured electrodes

Representative SEM micrographs of the nanostructured Pt/GC electrodes with different Pt loadings (Fig. 1a–c) illustrate the uniform size and the rather regular distribution of the Pt nanostructures (nanodisks), which appear as bright disks on the dark GC substrate. The Pt nanodisks (diameter ~65 nm, height ~20 nm) covered ~28%, ~13% and ~7% of the geometric area of the GC substrate (Table 1). Accordingly, the nanostructured samples were named HCL-28, HCL-13 and HCL-07. High-resolution images (see insets in Fig. 1a–c) demonstrate the absence of additional small Pt nanoparticles between the Pt nanodisks [2]. SEM images recorded before (Fig. 1a–c) and after (not shown) the electrochemical experiments revealed about identical Pt coverages, confirming that the Pt nanostructures were stable under present reaction conditions (see also Ref. [35]).

The electrochemical properties of the nanostructured Pt/GC electrodes were characterized by base cyclic voltammetry (CV) and pre-adsorbed CO_{ad} monolayer oxidation (CO_{ad} stripping). Cyclic voltammograms recorded on the different electrodes are depicted in Fig. 1d–g. They exhibit (i) hydrogen under-potential deposition (H_{upd}) features and PtO formation/reduction peaks typical for a polycrystalline Pt electrode, (ii) a gradual decrease in the charge in these features, and (iii) a gradual increase of the electrochemical features of glassy carbon [1,36,37] and of the double-layer charging current due to a larger exposed area of the substrate with decreasing Pt coverage (see Fig. 1a–c). The active surface area of the Pt and Pt/GC electrodes was determined by integration of the H_{upd} current in the negative-going scan (for details see Refs. [38,39]). To avoid interference with pseudocapacitive charging and quinone/hydroquinone redox features [40], which hinder a simple linear extrapolation of the double-layer current into the H_{upd} region, we additionally quantified the active surface area by oxidation of a saturated pre-adsorbed CO adlayer, monitoring the CO_2 formation rate, via the Faradaic current and on-line DEMS.

The CO_2 formation detected during the positive-going scan for the pc-Pt and the nanostructured Pt/GC electrodes is shown in Fig. 2 (bottom row). The active surface areas of the Pt/GC electrodes were calculated from the ratio of the CO_2 formation charge obtained during CO adlayer oxidation on the nanostructured surfaces and on the pc-Pt electrode (Table 1). In order to identify contributions from CO_2 fragmentation to the $m/z = 28$ ion current signal and separate these from CO consumption (see Section 3.3), we also measured the CO^+ signal. The resulting relative ion current of close to 10 % of that of the CO_2^+ signal agrees well with data reported previously [18].

3.2. CO adsorption kinetics

The CO adsorption kinetics was followed in potential-step experiments, stepping the potential from 0.06 to 1.0 V and back in CO-containing supporting electrolyte (1.0, 0.3 and 0.1 vol.% CO in Ar) on the different Pt and Pt/GC electrodes (pc-Pt, HCL-28, HCL-13 and HCL-07, (details see Section 2.2.) The resulting Faradaic current (upper row) and mass spectrometric current ($m/z = 44$, middle row, and $m/z = 28$, bottom row) transients at the three different CO concentrations are shown in Fig. 3.

Stepping the potential to 1.0 V causes a sudden spike-like increase of the measured current due to both pseudo-capacitive double layer charging and pre-adsorbed CO oxidation. This is followed by continuous CO oxidation. The latter is reflected by the simultaneous CO_2 formation and CO consumption. The currents obtained during continuous CO oxidation decrease proportionally with the CO concentration in solution. Furthermore, they are about similar for pc-Pt and the high loading nanostructured Pt electrode, but decrease significantly with further reduction of the Pt loading (see also Section 3.3).

After stepping back the electrode potential from 1.0 to 0.06 V, the CO_2 signal and hence the CO oxidation decreases steeply to the background level. The resulting current transients after stepping back the electrode potential from 1.0 to 0.06 V show an initial pseudo-capacitive spike, followed by a decaying negative current signal. The latter is caused by the increasing suppression of the hydrogen evolution at 0.06 V by the gradually developing CO adlayer, until the Pt surface is fully saturated with CO_{ad}. The CO_2 signal and hence the CO oxidation rate decreases steeply to the background level after stepping to 0.06 V. CO adsorption on the Pt surface, after stepping the electrode potential from 1.0 to 0.06 V, is quantitatively described by the simultaneously measured CO consumption [18,20]. Immediately after the potential step to 0.06 V, the $m/z = 28$ signal is even lower than that recorded during continuous CO oxidation at 1.0 V. This results from the fact that during CO oxidation intensity from the CO^+ fragment of CO_2 contributes to the $m/z = 28$ signal (see Fig. 2), but not during CO adsorption at 0.06 V. The highest CO consumption, in the first seconds after the potential step to 0.06 V on a CO-free Pt surface (see Fig. 3), is about proportional to the CO concentration (partial pressure). Most easily, this can be seen from the corresponding adsorption transients on the pc-Pt and HCL-28 samples. Upon continuous CO adsorption, the CO consumption gradually decreases with time due to the increasing CO_{ad} coverage. When the Pt surface is completely saturated with CO_{ad}, CO consumption is not possible any more and the $m/z = 28$ signal reaches the background level.

The adsorption rate and the temporal development of the CO_{ad} coverage were determined from the difference between the mass spectrometric $m/z = 28$ ion current and the background level (see Section 2.3). It should be noted that the CO_{ad} saturation coverage is slightly higher in the presence of CO in the solution than in CO free solution, due to a small reversible fraction of CO adsorption [28,41]. Since this difference is only about 2% of a monolayer in solutions containing CO concentrations of 1.0 vol.%, and even lower for more dilute CO-containing solutions, it was neglected in the present study.

The temporal evolution of the CO_{ad} coverage during CO adsorption on the polycrystalline Pt electrode and on the nanostructured

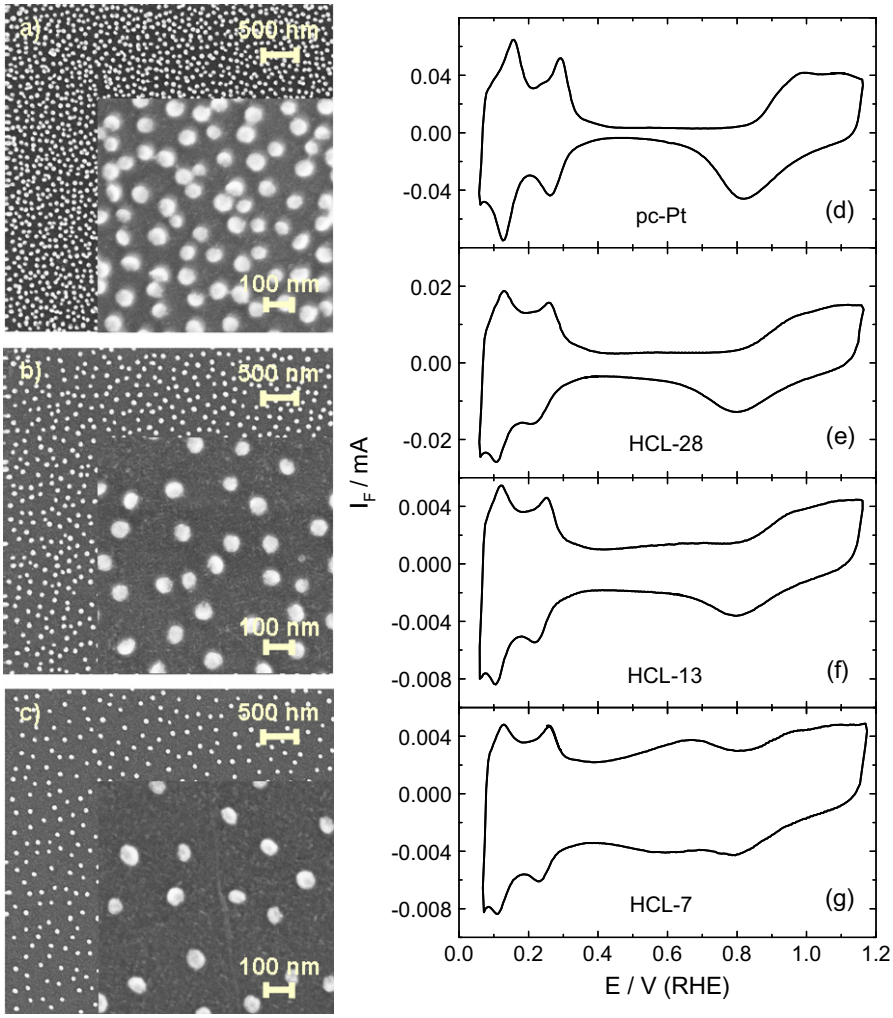

Fig. 1. Left panels: Representative large-scale (a–c) and high-resolution (corresponding insets) SEM micrographs of the nanostructured Pt/glassy carbon model electrodes fabricated by Hole-mask Colloidal Lithography (HCL): (a) HCL-28 (Pt coverage ~28 %), (b) HCL-13 (Pt coverage ~13 %), and (c) HCL-07 (Pt coverage ~7 %); right panels: the base cyclic voltammograms of a smooth polycrystalline Pt (d) and the nanostructured Pt electrodes (e–g) with different Pt coverages. Exposed electrode area 0.28 mA cm^{-2}, Ar saturated 0.5 M H_2SO_4, electrolyte flow rate 10 μL s^{-1}, potential scan rate 100 mV s^{-1}, room temperature.

Table 1
SEM and electrochemical characterization of nanostructured Pt/GC electrodes.

Sample	Pt coverage (%)	Particle diameter (nm)	Particle density (μm^2)	Inter-particle distances (nm)	Active Pt surface area (cm^2)	Relative active Pt surface areas (%)
pc Pt	100	–	–	–	0.671	100.0
HCL-28	28	66 ± 21	76	105	0.180	26.9
HCL-13	13	65 ± 12	38	151	0.063	9.4
HCL-07	7	67 ± 9	19	213	0.037	5.6

Pt/GC electrodes from electrolyte solutions saturated with 1.0, 0.3 and 0.1 vol.% CO mixtures with Ar is plotted in Fig. 4a–d. The time required for reaching the saturation CO_{ad} coverage depends on the CO concentration and on the Pt loading. It is significantly shorter at higher CO concentrations and lower Pt loading, respectively. For low Pt loading and low CO partial pressures, the scatter in the coverage–time plot increases significantly when approaching the saturation coverage due to the rapidly decreasing signal intensity and signal-to-noise ratio in the in $m/z = 28$ current signal (Fig. 3, 2nd row).

The corresponding CO adsorption rates are plotted vs. time in Fig. 4e–h. In all cases, the CO adsorption rate is highest initially and decreases with time to zero, at a rate depending on the CO concentration and Pt loading. The decrease of the adsorption rate with time reflects the influence of the growing CO_{ad} coverage on the adsorption process, which will be discussed in more detail below. The faster CO adsorption at higher CO concentrations can simply be explained by the increasing CO diffusion to the surface at higher CO concentration gradients. The CO adsorption rates, in terms of ML s^{-1}, are generally higher on the nanostructured electrodes, by up to a factor of ~10 for the lowest Pt density sample (HCL-07) compared to the pc-Pt electrode. This, in contrast, cannot be explained within a model of a purely planar (1D) diffusion geometry, since in that case the total CO flux to the electrode and the flux density relative to the geometric surface area of the electrode are independent of the geometric Pt coverage. Instead, it indicates that

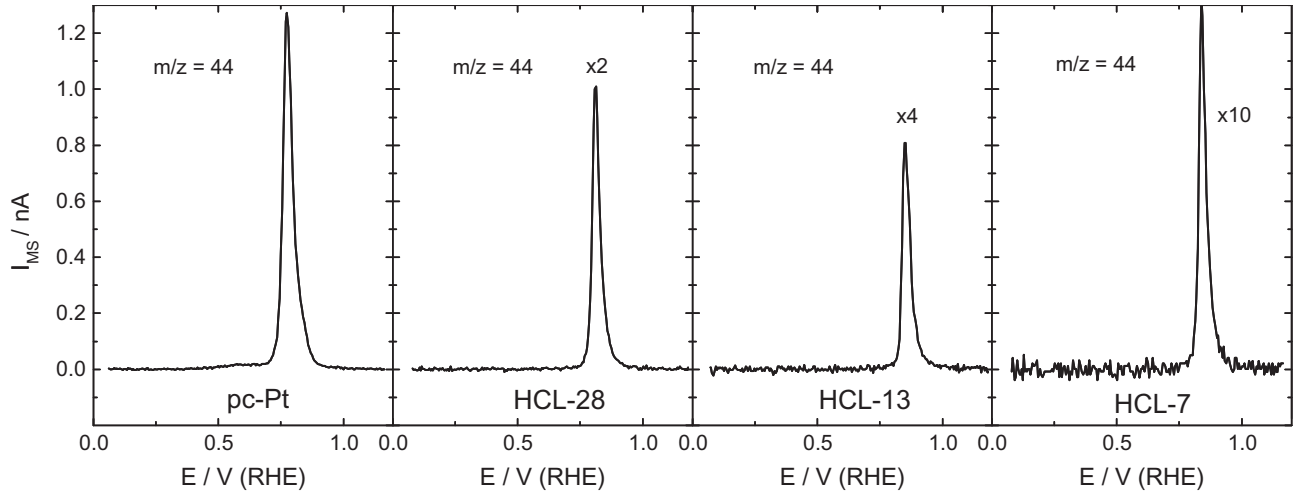

Fig. 2. CO_2^+ ion currents during oxidation of pre-adsorbed CO saturated adlayer on a smooth polycrystalline Pt and on nanostructured Pt/GC electrodes (see Figure). Exposed electrode area 0.28 cm^2, Ar saturated 0.5 M H_2SO_4, electrolyte flow rate 10 μL s^{-1}, potential scan rate 10 mV s^{-1}, room temperature.

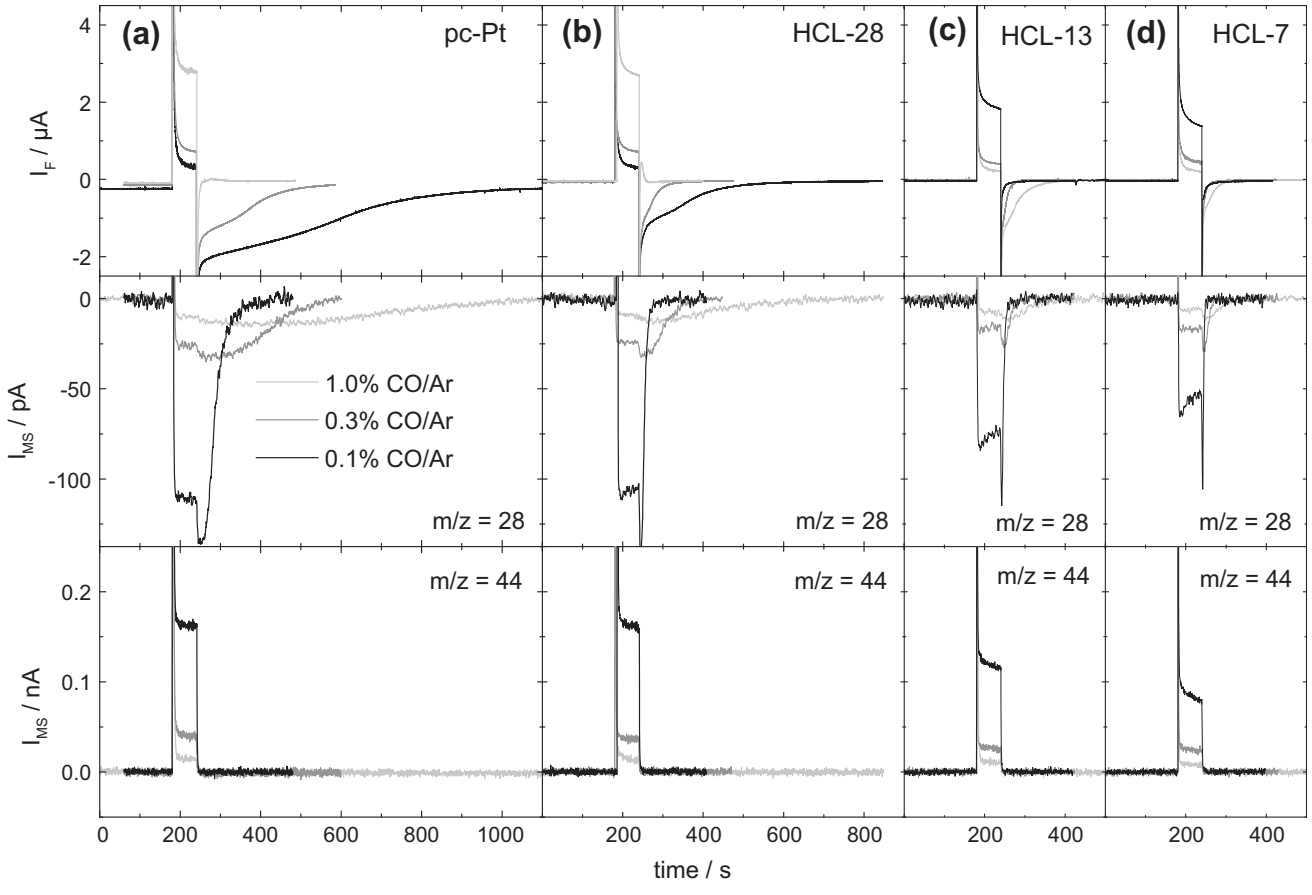

Fig. 3. Faradaic and mass spectrometric (m/z = 44, middle row, and m/z = 28, bottom row) current transients at three different CO concentrations (1.0 – light grey, 0.3 – grey and 0.1 – black vol.% CO mixtures in Ar in 0.5 M H_2SO_4) for polycrystalline Pt (a) and nanostructured Pt/GC electrodes with different Pt coverage (b–d), see Figure). Experimental protocol: constant applied potentials of E_{init} = 60 mV (t_{init} = 120 s), E_{ox} = 1.0 V (t_{ox} = 60 s) and E_{ads} = 60 mV ($t_{ads} \approx$ 3–15 min depending on the concentration of CO and Pt coverage), electrolyte flow rate 10 μL s^{-1}.

for the nanostructured Pt/GC electrodes, contributions from hemispherical (3D) diffusion above individual Pt nanodisks modify the planar diffusion behavior, while the latter is still dominant further away from the electrode. Hence, for these electrodes and in particular for lower Pt loading, the diffusion characteristics changed from purely planar diffusion to a combination of planar and hemispherical diffusion (planar-plus-hemispherical diffusion) [6,31–33]. This results in an increasing mass transport (arrival rate) of CO per Pt nanodisk and hence per Pt surface atom, and the effect scales with decreasing density or increasing separation of the

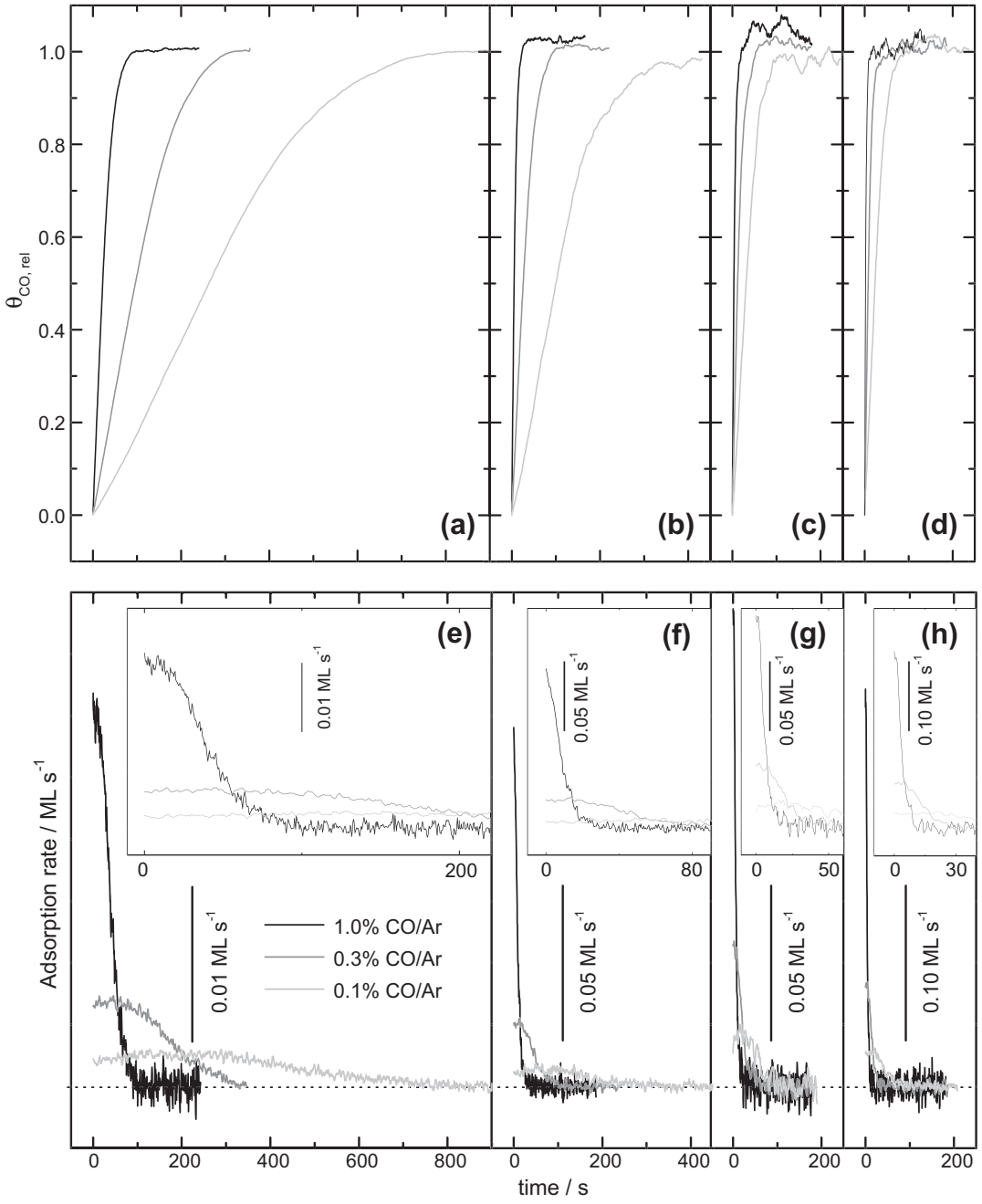

Fig. 4. Upper panel (a–d): Temporal evolution of the CO_{ad} coverage during CO adsorption on a polycrystalline Pt electrode (a) and nanostructured Pt/GC electrodes with different Pt coverage (b–d) (see figure) from supporting electrolyte solutions saturated with 1.0 (black), 0.3 (dark grey) and 0.1 (light grey) vol.% CO mixtures with Ar in 0.5 M H_2SO_4, electrolyte flow rate 10 μL s^{-1}. Lower panel (e–h): Temporal evolution of the CO adsorption rate on the respective electrodes in the different CO containing solutions (see upper caption). Insets show the initial phase on an expanded time scale.

individual Pt nanostructures in the order HCL-28 < HCL-13 < HCL-07). The increase in CO mass transport to a individual Pt nanodisk cannot exceed, however, the limits given by planar diffusion further away from the electrode surface. Therefore, the increase of the Pt coverage normalized initial adsorption rate is limited to a factor $^1/_{\text{Pt coverage}}$, which would result in a constant (absolute) CO adsorption rate, independent of the Pt coverage.

The temporal evolution of the CO adsorption rates (from Fig. 4b) with the CO_{ad} coverage (from Fig. 4a) for the different samples and CO concentrations is shown for the pc-Pt and the HCL-07 in Fig. 5a. The general shapes of these curves, which directly reflect the influence of the increasing CO_{ad} coverage on the overall CO adsorption characteristics, are rather similar for the different electrodes and CO concentrations, with a small decay up to a CO_{ad} coverage of ~0.5, followed by a steep(er) decay to zero at higher coverages, until reaching saturation at $\theta_{CO} = 1$. The considerable variation in the absolute values of the adsorption rates between the different electrodes and CO concentrations follows that of the time-dependent CO adsorption rates (Fig. 4a, see above).

More information on the influence of the CO adlayer on the adsorption process comes from the relation between the sticking coefficient $s(\theta)$ for CO adsorption and the CO_{ad} coverage. $s(\theta)$ defines the probability that a CO molecule hitting the active electrode surface with a given CO_{ad} coverage will adsorb. This relation has been investigated for a number of adsorption models such as Langmuir adsorption kinetics of different orders [42]. Hence,

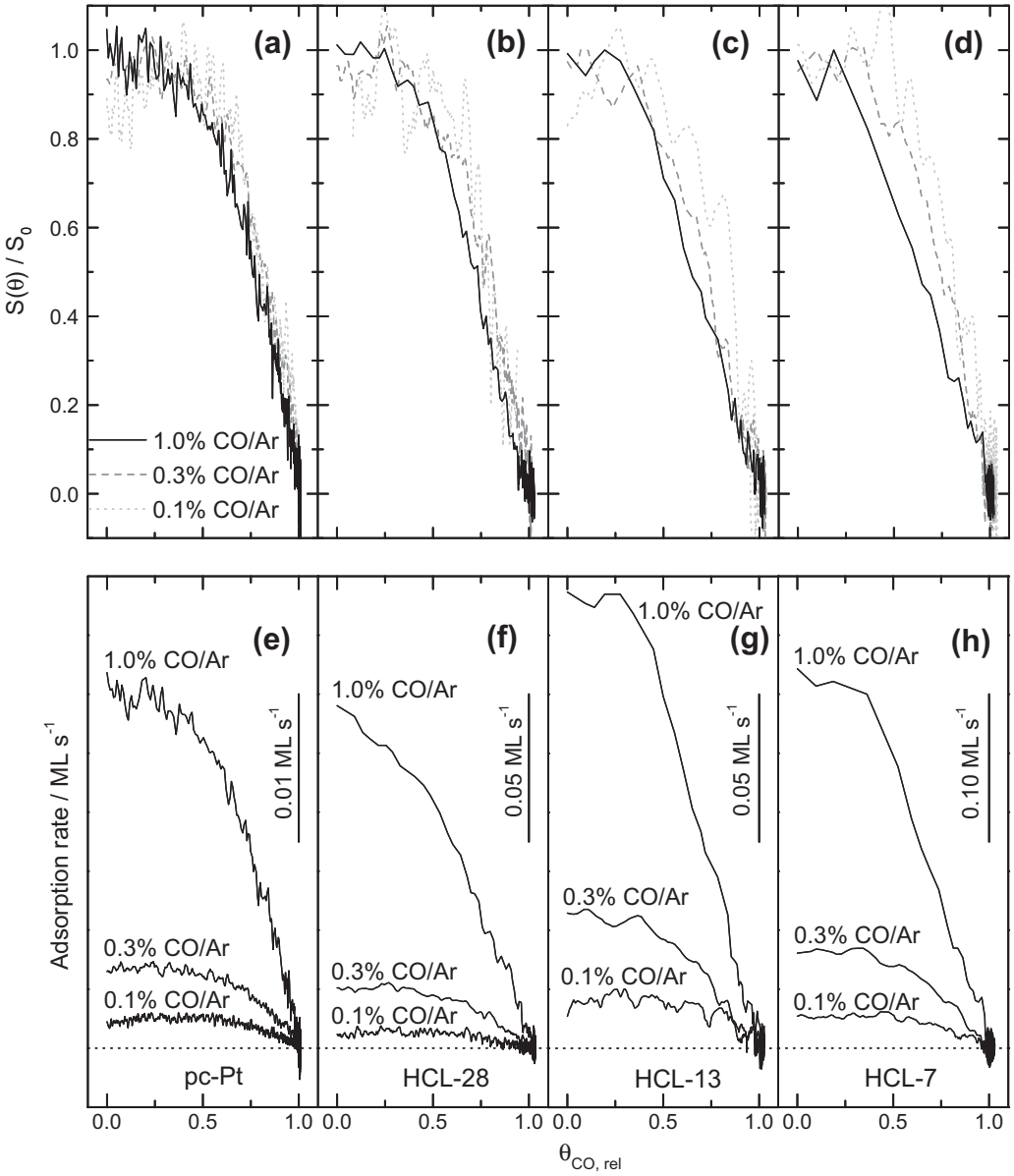

Fig. 5. Upper panel (a–d): CO adsorption rates (data from Fig. 3a–d) plotted vs. the CO_{ad} coverage (Fig. 4a–d) on a polycrystalline Pt electrode (a) and nanostructured Pt/GC electrodes with different Pt coverage (b–d) (see Figure) in the different CO containing solutions. Lower panel (e–h): Relative, effective sticking coefficients $s_{eff,rel}$ plotted vs. the relative CO_{ad} coverage on the respective electrodes (data extracted from Fig. 3, $m/z = 28$ ion current). The signals for the HCL-13 and HCL-07 samples in 0.1 vol.% CO mixtures are smoothened by averaging due to their poor signal-to-noise ratio.

comparison between the experimental relation and modeled ones can provide information on the microscopic adsorption behavior. In contrast to the conditions at the solid–gas interface, however, we do not know the exact number of collisions per second between CO molecules and the electrode surface at the solid–liquid interface. Therefore, the sticking coefficient derived in the present measurements will be denoted as effective sticking coefficient, $s_{eff}(\theta)$. It describes the probability that a CO molecule arriving at the electrode surface will eventually be adsorbed, after an unspecified number of collisions/attempts. It can be derived from the slope of the adsorption rate–coverage relation in Fig. 5a.

$$s_{eff}(\theta) = \frac{dn_{ad}(\theta)}{dF} \quad (1)$$

Since we also do not know the absolute number of incoming CO molecules, F, we will determine the relative effective sticking coefficient $s_{eff,rel}(\theta) = s_{eff}(\theta)/s_{eff,0}$ where $s_{eff,0}$ describes the effective sticking probability in the limits of zero coverage. Accordingly, we obtain $s_{eff,rel}(\theta = 0) = 1$. The relative effective sticking coefficient $s_{eff,rel}(\theta)$ is plotted vs. the relative CO_{ad} coverage in Fig. 5b. Because of their poor signal-to-noise ratio, the signals for the samples with low Pt densities (HCL-13 and HCL-07) and low CO concentrations (0.1 vol.% CO) are smoothed by averaging.

The shapes of the $s_{eff,rel}(\theta)$ vs. θ_{CO} relations are essentially identical for the different electrodes and CO concentrations. They also resemble those found for a carbon-supported Pt catalyst thin-film electrode [18] or Pt film electrodes prepared by electroless deposition [20], both of which can be considered as high Pt loading electrodes. Starting at unity at $\theta_{CO} = 0$, the relative effective sticking coefficient decreases only little up to CO_{ad} coverages of ~0.5, and then decays almost linearly to zero with further increasing CO_{ad} coverage.

The sticking coefficient profiles clearly differ from the linear decay of the (relative) sticking coefficient with increasing CO_{ad} as

expected for simple Langmuir adsorption kinetics. The deviation from a linear correlation can most easily be explained by a precursor-type adsorption kinetics, where the molecules landing on the partly blocked surface can still migrate over the surface and make several attempts for finding an unoccupied site for adsorption, which indeed is often observed for CO adsorption at the gas–solid interface. In an electrochemical environment, however, a direct conclusion on a precursor type adsorption behavior is not possible just from the characteristics of the adsorption kinetics. A similar behavior can also result from the different transport conditions. During adsorption from a liquid, CO molecules dissolved in the liquid phase may repeatedly hit the surface after an unsuccessful adsorption attempt, i.e., each molecule undergoes several collisions with the surface as long as it stays in the stagnant diffusion layer. In contrast, for adsorption at the solid–gas interface under ultrahigh vacuum conditions, ballistic motion is dominant and CO molecules will hit the sample surface only once before being pumped away. The multiple collision characteristics at the solid–liquid interface will result in characteristics of the adsorption kinetics similar to those of precursor-type adsorption at the solid–gas interface even in the absence of a microscopic precursor [18,20].

For the nanostructured Pt/GC samples, the general adsorption characteristics are similar to those observed on the pc-Pt sample. The development of the relative effective sticking coefficient with CO_{ad} coverage is essentially independent of the Pt coverage and CO concentration. Except for the increasingly higher adsorption rate, caused by the transition from planar diffusion to combined planar-plus-hemispherical diffusion (see discussion above), the adsorption characteristics are hardly affected by mass transport. This indicates that, as one would expect, the actual adsorption process and also its correlation with mass transport effects are identical on a molecular scale on the different electrodes. For lower Pt nanostructure densities and higher CO concentrations, i.e., shorter time for the saturation of the surface with CO, the experimental accuracy decreases, and the smear-out of the CO concentration profile upon starting CO adsorption results in an initially slower adsorption process (lower CO concentration) than under ideal conditions (stepwise start of the CO concentration in the electrolyte), which in turn leads to an apparent shift in the decrease of the relative, effective sticking coefficient with CO_{ad} coverage (see Fig. 5d). This effect is most pronounced for the highest CO concentration and low Pt coverages, and becomes increasingly less significant for higher Pt coverages and lower CO concentrations.

3.3. Continuous CO oxidation

To quantitatively assess mass transport effects on the kinetics of the continuous CO oxidation reaction, we recorded oxidation transients at different potentials (1.0–1.3 V) on the pc-Pt electrode and on the nanostructured Pt/GC electrodes in CO containing solution (1% CO/Ar) (exp. protocol see Section 2.2). The resulting Faradaic (Fig. 6b) and mass spectrometric currents (Fig. 6c and d) are shown in Fig. 6, together with a schematic representation of the potential variation with time (Fig. 6a). The oxidation potential was first stepwise increased from 1.0 to 1.3 V, and then decreased again to 1.0 V to exclude effects of the history of the previous potential variations, which may result in the formation of a Pt oxide layer of different thickness [43,44].

The general shapes of the transients can be characterized as follows. The measured current transients (Fig. 6b) exhibit a steep initial spike upon stepping the potential to the reaction potential, a decay with time to quasi-steady-state oxidation rates (for exact values see Table 2), and negative current spikes when stepping the electrode potential back to 0.06 V, as discussed in Section 3.2. The corresponding mass spectrometric current transients for CO_2 formation during CO oxidation (Fig. 6d) purely reflect the CO oxidation rate. Stepping the potential to the reaction regime also results in a steep initial spike of the mass spectrometric signal, which we attribute to the oxidation of CO_{ad} pre-adsorbed at 0.06 V, followed by a slow decay of the CO_2 signal to a new steady-state value. Stepping the potential back to 0.06 V, the CO_2 formation rate drops instantaneously to its background level and remains there (Fig. 6d). This is different from the negative current spike in the current response (Fig. 6b) upon returning to 0.06 V.

The mass spectrometric $m/z = 28$ ion current transients (Fig. 6c) exhibit a complex behavior upon stepping the electrode potential, which is caused by the fact that CO consumption may either result from CO oxidation at higher potentials or from adsorption at 0.06 V. While the CO oxidation rate will approach a finite steady-state value at the reaction potentials used here, the adsorption rate will approach zero upon saturation of the surface at 0.06 V (Fig. 6b and d).

When stepping to the oxidation potential, the $m/z = 28$ ion current passes through a steep spike, which is caused by the CO^+ fragment of CO_2 formed upon oxidation of pre-adsorbed CO. During continuous CO oxidation, the $m/z = 28$ ion current largely mirrors the $m/z = 44$ signal. Returning to the initial potential of 0.06 V, the $m/z = 28$ signal decreases with the slope depending on the Pt coverage (Fig. 6c), equivalent to an increasing CO consumption, whereas the CO_2 formation stops immediately and stays at the background level (Fig. 6d). The difference between CO consumption due to CO oxidation (1.0–1.3 V) and due to CO adsorption (0.06 V) becomes more pronounced with decreasing Pt nanostructure and increasing oxidation potential (Fig. 6c). The initial CO consumption, immediately after stepping the potential back to 0.06 V, corresponds to the CO adsorption rate on a clean Pt surface. This can be taken as a mass transport limit for the CO flux to the electrode surface achieved under present transport conditions (electrolyte flow rate and CO concentration). The lower CO consumption for continuous CO oxidation at higher potentials indicates a decrease in the oxidation rate due to kinetic limitations. This will be discussed in more detail below.

The variation of the steady state Faradaic currents and of the $m/z = 44$ (b) and $m/z = 28$ (c) ion currents with Pt coverage is summarized in Fig. 7a–c and in Table 2 (data taken from Fig. 6). The $m/z = 28$ ion current signals are corrected by accounting for contributions from CO_2 fragmentation (10% of the CO_2 signal). The main features are:

(i) The steady-state Faradaic current (Fig. 7a) and the $m/z = 44$ ion current (Fig. 7b) decrease with decreasing Pt coverage below a critical Pt coverage at identical reaction potentials. For instance, CO oxidation at 1.0 V leads to about similar steady-state currents for polycrystalline Pt and the high-loaded nanostructured HCL-28 sample. Upon a further decrease in the Pt coverage, however, the Faradaic current decreases, as evident for the lower density nanostructured Pt/GC samples (HCL-13 and HCL-07) at the same potential.

(ii) The decrease of the CO oxidation rate with decreasing Pt coverage is more pronounced for higher reaction potentials. While at 1.0 V it decreases by about 57% from pc-Pt to HCL-07, the equivalent decrease is 84% at 1.3 V.

(iii) The steady-state Faradaic current (Fig. 7a) and the $m/z = 44$ ion current (Fig. 7b) decrease with increasing oxidation potential for identical Pt coverage. This decrease is more pronounced for lower Pt coverages. On pc-Pt, the oxidation rate decreased by ~32% upon increasing the reaction potential from 1.0 V to 1.3 V, while on the HCL-07 sample the oxidation rate decreased by about 75% under identical experimental conditions.

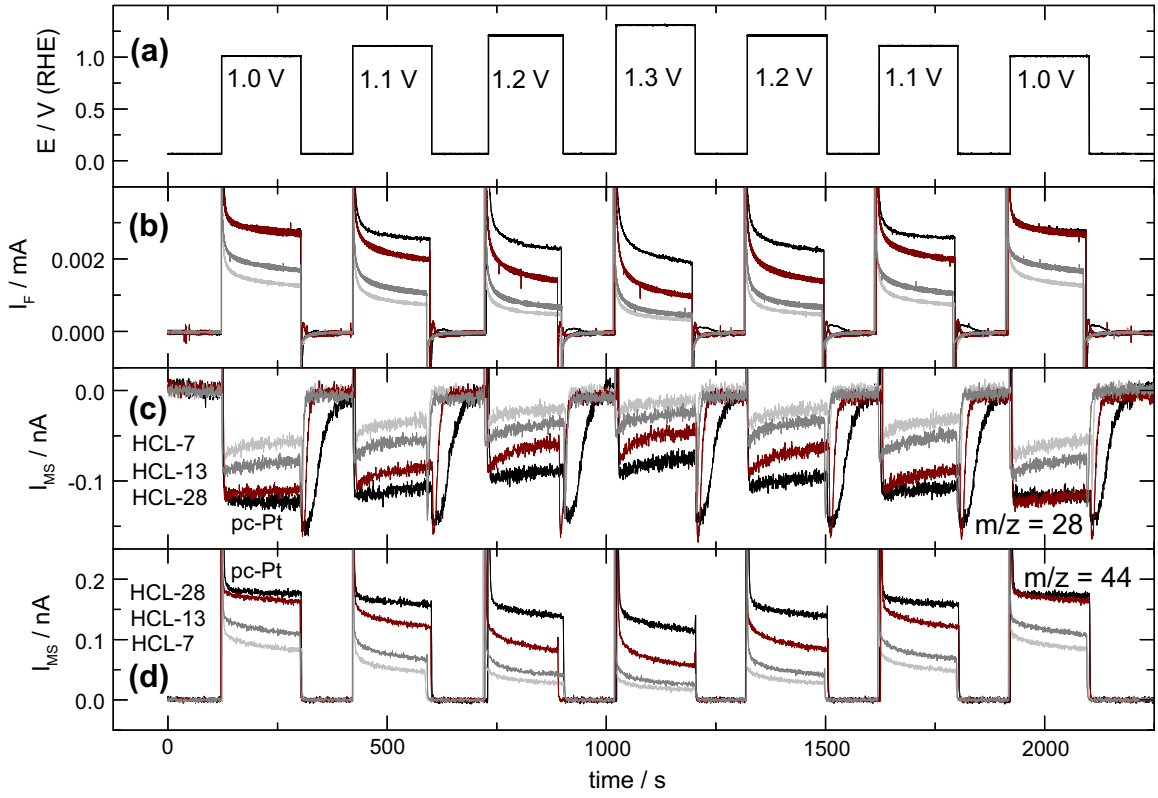

Fig. 6. Continuous potentiostatic electrooxidation of CO on a polycrystalline Pt (black) and on nanostructured Pt/GC electrodes with different Pt coverages (see Figure) in 1 vol.% CO/Ar in 0.5 M H_2SO_4 solution. Electrolyte flow rate 10 μL s^{-1}: (a) applied potential, (b) Faradaic currents, (c) CO consumption: mass spectrometric currents at $m/z = 28$, and (d) CO_2 formation: mass spectrometric currents at $m/z = 44$.

Table 2
CO oxidation rates in μA (values for stepwise increased potential) of pc-Pt and the different nanostructured Pt/GC electrodes after 3 min at various potentials.

Sample/potential	1.0 (V)	1.1 (V)	1.2 (V)	1.3 (V)
pc Pt	2.83	2.61	2.4	1.92
HCl-28	2.74	2.02	1.39	1.0
HCl-13	1.73	1.05	0.65	0.43
HCl-07	1.2	0.69	0.45	0.31

(iv) Stepwise lowering the potential back to 1.0 V results in oxidation rates similar to those obtained when increasing the potential (Fig. 7a and b), underlining that the potential-induced changes in the activity are reversible under steady state conditions. Similar trends apply also for the CO consumption during CO oxidation, which decreases with increasing reaction potential and decreasing Pt coverage (Fig. 7c).

On a quantitative scale, the CO consumption during continuous CO oxidation at 1.0 V on the pc-Pt electrode is identical to the initial CO consumption during adsorption, which was purely mass transport limited (see Section 3.2). Therefore, continuous CO oxidation on the pc-Pt electrode at 1.0 V and under present transport conditions can be assumed to be mass transport limited with negligible kinetic limitations, in agreement with the proposal in Ref. [27]. The latter become increasingly more pronounced with decreasing Pt loading or increasing electrode potential. To discriminate between kinetic and mass transport limitations in continuous CO oxidation, we normalized the Faradaic currents vs. the active Pt surface area, since the kinetically limited Faradaic currents are proportional to the active Pt surface area. (Note that for the present electrodes there is essentially no difference between active surface area normalization (oxidation rate) and Pt coverage normalization (adsorption rate), since the two quantities are linearly correlated.) The resulting plots of the CO oxidation current densities and CO_2 formation/CO consumption ion current densities (active surface areas see Table 1) are plotted in Fig. 7d–f. The transport limited maximum CO oxidation current densities, derived from the (purely mass transport limited) initial CO adsorption rates at 0.06 V (see Section 3.2), are included as dashed lines in Fig. 7d as benchmarks to distinguish between mass transport effects and kinetic limitations for the different samples and reaction potentials. If CO_{ad} oxidation were solely mass transport limited, the CO_2 formation rate should reach the value given by the dashed line. These plots lead to the following main conclusions.

(i) The CO oxidation current density deviates increasingly from the mass transport limited maximum CO oxidation current density with decreasing Pt coverage at 1.0 V reaction potential. While for the pc-Pt electrode it is essentially identical to the (mass transport limited) theoretical maximum CO oxidation current density, it deviates already for the HCL-28 electrode (ca. 85% of the mass transport limited value), and is significantly smaller than the mass transport limited values for the HCL-13 (55%) and HCL-07 (45%) samples.
(ii) In agreement with the increase in CO flux to the individual nanodisks, which increases by about one order of magnitude when going from the pc-Pt electrode to the HCL-07 electrode, the active Pt surface area normalized oxidation rate increases by a factor of 8 at 1.0 V but only by a factor of 3 at 1.3 V.
(iii) For all samples, the deviations from the mass transport limited maximum CO oxidation current (dashed lines) become more pronounced with increasing oxidation potential and

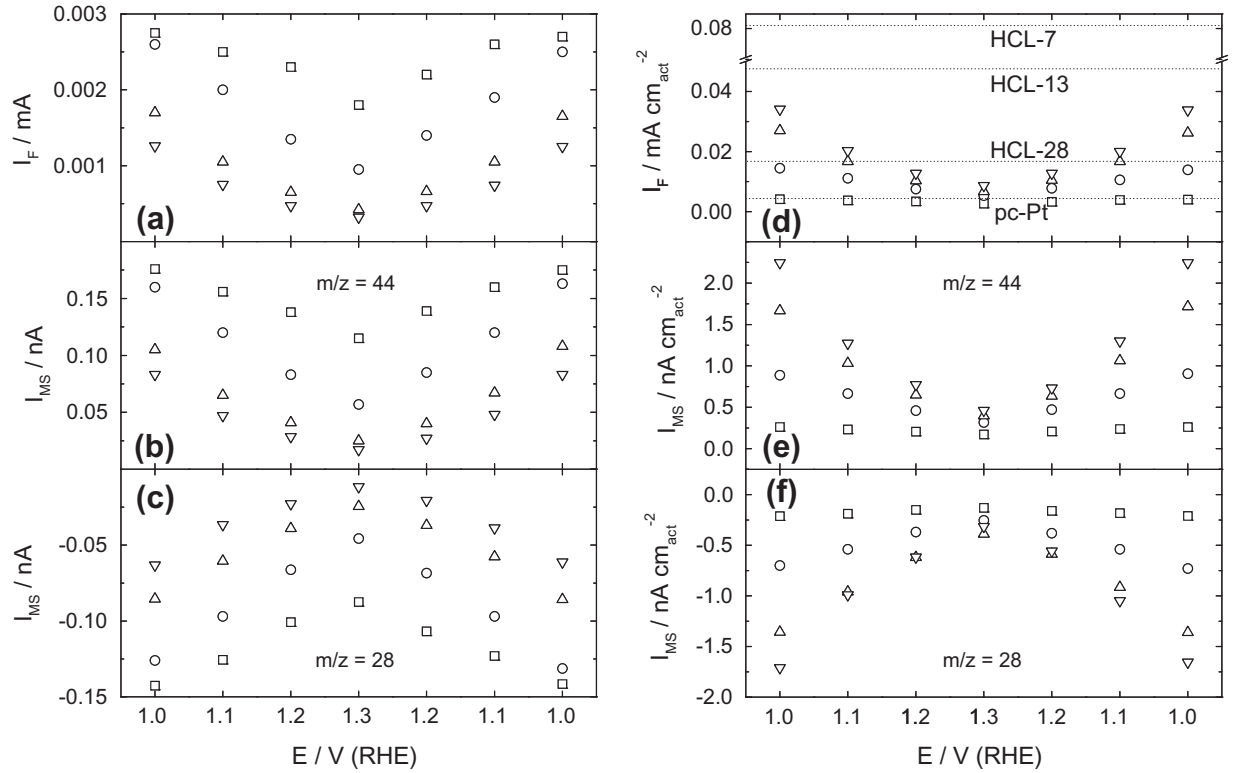

Fig. 7. Left panel (a–c): Steady-state Faradaic (a), $m/z = 44$ (b) and $m/z = 28$ (c) ion currents obtained after ca. 3 min continuous electrooxidation of CO (1% CO in Ar) over polycrystalline Pt (squares) and nanostructured Pt/GC electrodes with different Pt coverages (see Figure) plotted vs. the applied potentials (data extracted from Fig. 6). Electrolyte flow rate 10 μL s^{-1}. (Note: The $m/z = 28$ ion current signal in Fig. 6c is corrected accordingly by accounting for 10% fragmentation from the CO_2 formed.). Right panel (d–f): As above, but using current densities normalized to the active Pt surface area (see Table 1).

(iv) The decrease in CO oxidation current density with increasing reaction potential is increasingly more pronounced at lower Pt loadings. Correspondingly, the differences in the current densities gradually vanish with increasing oxidation potential, approaching close to similar values at 1.3 V.

The latter was not obvious from the measured Faradaic currents in Fig. 7a (see also Table 2), where the kinetic effects are superimposed with Pt loading effects. Hence, at 1.3 V and under present transport conditions, the current density is predominantly limited by kinetic effects. These results are qualitatively in line with the recent finding of a more efficient suppression of the potentiodynamic CO bulk over nanostructured Pt/GC electrodes with decreasing Pt nanostructure coverage [9]. Furthermore, this plot demonstrates that also for the pc-Pt electrode the mass transport limited CO oxidation current (reaction current at 1.0 V) is not much larger than the kinetic limitation at 1.3 V. This implies that under present transport conditions, with 1.0% CO and lower concentrations in the gas phase dissolved in the electrolyte, an extended electrode surface just still provide sufficient amounts of oxy-species required for reaction with approaching CO such that the steady state CO_{ad} coverage is low. This will of course be different for higher fluxes of CO to the electrode surface (higher CO concentration or faster mass transport, e.g., in a rotating disk electrode configuration).

Kinetic limitations in the CO oxidation reaction can either result from surface blocking by adsorbed species, e.g., from higher steady-state coverages of CO_{ad} (low potentials) or from adsorbed oxy-species, or from a potential- or surface phase dependent decrease of the activity at more positive potentials. Surface blocking by CO_{ad} can be ruled out under these conditions, since recent *in situ* IR spectroscopy measurements, performed under comparable transport conditions, showed no evidence of adsorbed CO species under these conditions [29]. The present data do not allow us, however, to discriminate between the other two possibilities, surface blocking by adsorbed oxy-species or a potential induced decay in activity. Potential-induced Pt surface blocking due to PtO formation at $E > 1.0$ V was postulated to be a factor responsible for decreasing the number of available free sites required for CO_{ad} adsorption, which leads to a corresponding decrease in CO oxidation rate [27].

The data presented in this contribution allowed to quantitatively distinguish between kinetic limitations and transport effects. A quantitative understanding on a microscopic scale, however, will require extensive modelling and simulations of the diffusion and migration processses in the stagnant diffusion layer above the electrode surface. Using a three-step reaction mechanism for continuous CO oxidation, which includes the influence of surface coverages on adsorption, desorption, and oxidation of CO, coupled with 2D and 3D mass transport models, allowed us to numerically simulate and quantitatively predict the reaction behavior on a (non-structured) polycrystalline Pt electrode during a potentiodynamic scan in a dual thin-layer flow cell as a first step [45].

4. Summary and conclusions

We have studied the influence of mass transport on the adsorption and continuous electro-oxidation of CO under well-defined transport and reaction conditions in a thin-layer flow cell using a novel approach. The use of nanostructured, planar Pt/GC electrodes consisting of regular arrays of Pt nanodisks (∅ 60 nm) on a planar glassy carbon substrate, which were fabricated via Hole-mask Colloidal Lithography, allowed us to modify the transport and

diffusion characteristic in a controlled way and over a wide range by varying the CO concentration and the density of the Pt nanodisks, and this way discriminate between transport effects and limitations arising from the adsorption/reaction kinetics. CO adsorption and oxidation were monitored by following the Faradaic current, the consumption of CO and the formation of CO_2 by electrochemical and on-line mass spectrometric measurements.

1. CO adsorption on clean, CO_{ad} free Pt or Pt nanodisk surfaces (initial adsorption rate) is purely mass transport limited. This is indicated by the similar absolute adsorption rates observed in the range of medium to high Pt nanodisk coverages, on the pc-Pt (100% coverage) and on the HCL-28 (28% coverage) electrodes. Diffusion through the essentially unmodified planar diffusion zone controls the transport to the electrode, leaving the absolute adsorption rate constant. In this coverage range, the decay in Pt coverage is compensated by the increasing Pt coverage normalized adsorption rate. For lower Pt coverages, this is no more the case and the absolute adsorption rate decreases despite of the further increasing Pt coverage normalized adsorption rate.
2. The adsorption rate, normalized to the surface area covered by the Pt nanodisks, increases continuously with decreasing Pt coverage, by up to one order of magnitude for going from the pc-Pt electrode to the HCL-07 (7% Pt coverage) electrode. This reflects a gradual transition from purely planar diffusion characteristics, above the pc-Pt electrode, to combined planar-plus-hemispherical diffusion characteristics over nanostructured Pt/GC electrodes, where hemispherical diffusion zones above individual Pt nanodisks lead to an increased flux of CO molecules to the individual nanodisks.
3. The CO_{ad} coverage dependence of CO adsorption rate and sticking coefficient, with a slow decrease up to 50% CO_{ad} coverage and a steep decline in the high coverage regime, down to zero at saturation, reflects the special situation in a diffusion controlled system, where in contrast to the single-hit situation at the solid–gas interface (under UHV conditions) a CO molecule approaching the electrode surface can make multiple encounters attempting to find and adsorb on an empty adsorption site as long as it is in the diffusion layer, before it is eventually transported away from the surface region. The present data are not sufficient to conclude on adsorption via a precursor state, as it is typical for CO adsorption on metal surfaces at the solid–gas interface, although they are compatible with it and this appears likely.
4. Continuous CO oxidation measurements at constant reaction potentials between 1.0 and 1.3 V showed: (i) that the reactivity under steady-state conditions, defined by the active Pt surface area normalized Faradaic current for CO oxidation or the similarly normalized CO consumption/CO_2 formation rates, decreases with increasing potential and/or increasing Pt coverage; (ii) In the limit of low CO flux densities and high reactivities, as obtained for the extended pc-Pt electrode for reaction at 1.0 V, the CO oxidation rate is identical to the initial CO adsorption rate on the same electrode surface, and hence is controlled by transport limitations; (iii) at constant potential of 1.0 V and with decreasing Pt nanodisk coverage, i.e., increasing mass transport to the Pt surface, kinetic limitations set in and become increasingly dominant, resulting in significantly lower oxidation rates compared to the mass transport limited theoretical rates (up to 58% lower for the HCL-07 electrode). At higher potentials, the CO oxidation rate becomes increasingly lower than the corresponding CO adsorption rates (this is true for both the absolute rates and the surface area normalized rates), and this potential dependent deviation increases with decreasing Pt nanostructure coverage. At 1.3 V, similarly active Pt surface area normalized reaction rates are reached for all electrodes, indicating that under these conditions the reaction is dominated by kinetic limitations.

Acknowledgements

This work was supported by the Baden–Württemberg Stiftung via the 'Kompetenznetz Funktionale Nanostrukturen' (Project B9). The work at Chalmers was performed at the Competence Centre for Catalysis, hosted by Chalmers University of Technology and financially supported by the Swedish Energy Agency and the member companies: AB Volvo, Volvo Car Corporation, Scania CV AB, GM Powertrain Sweden AB, Haldor Topsøe A/S and The Swedish Space Corporation. The Swedish Energy agency also supported the work via the Nano-See Project. The authors are grateful to A. Minkow (Institute of Micro- and Nanomaterials, Ulm University) for SEM measurements and to S. Tiedemann (Institute of Surface Chemistry and Catalysis, Ulm University) for developing the software for the quantitative SEM image evaluation.

References

[1] M. Gustavsson, H. Fredriksson, B. Kasemo, Z. Jusys, C. Jun, R.J. Behm, J. Electroanal. Chem. 568 (2004) 371.
[2] Y.E. Seidel, M. Müller, Z. Jusys, B. Wickman, P. Hanarp, B. Kasemo, U. Hörmann, U. Kaiser, R.J. Behm, J. Electrochem. Soc. 155 (2008) K171.
[3] P. Hanarp, D. Sutherland, J. Gold, B. Kasemo, Colloids Surf. A 214 (2003) 23.
[4] H. Fredriksson, Y. Alaverdyan, A. Dmitriev, C. Langhammer, D.S. Sutherland, M. Zäch, B. Kasemo, Adv. Mater. 19 (2007) 4297.
[5] A. Schneider, L. Colmenares, Y.E. Seidel, Z. Jusys, B. Wickman, B. Kasemo, R.J. Behm, Phys. Chem. Chem. Phys. 10 (2008) 1931.
[6] Y.E. Seidel, A. Schneider, Z. Jusys, B. Wickman, B. Kasemo, R.J. Behm, Faraday Discuss 140 (2008) 167.
[7] Y.E. Seidel, A. Schneider, Z. Jusys, B. Wickman, B. Kasemo, R.J. Behm, Langmuir 26 (2010) 3569.
[8] Y.E. Seidel, Z. Jusys, R. Lindström, M. Stenfeldt, B. Kasemo, K. Krischer, Chem. Phys. Chem. 11 (2010) 1405.
[9] R. Lindström, Y.E. Seidel, Z. Jusys, M. Gustavsson, B. Kasemo, R.J. Behm, J. Electroanal. Chem. 644 (2010) 90.
[10] J.C. Campuzano, in: D.A. King, D.P. Woodruff (Eds.), Chemisorption Systems, vol. 3A, Elsevier Publishers, Amsterdam, 1990.
[11] I. Villegas, N. Kizhakevariam, M.J. Weaver, Surf. Sci. 335 (1995) 300.
[12] M.T.M. Koper, A.P.J. Jansen, R.A. van Santen, J. Chem. Phys. 109 (1998) 6051.
[13] S.A. Wasileski, M.T.M. Koper, M.J. Weaver, J. Phys. Chem. B 105 (2001) 3518.
[14] A. Cuesta, A. Couto, A. Rincón, M.C. Perez, A. Lopez-Cudero, C. Gutierrez, J. Electroanal. Chem. 586 (2006) 184.
[15] M. Watanabe, H. Uchida, in: M.T.M. Koper (Ed.), Fuel Cell Catalysis: A Surface Science Approach, Wiley & Sons, Chichester, 2008 (Chapter 10).
[16] Fuel Cell Catalysis: A Surface Science Approach, M.T.M. Koper (Ed.), Wiley & Sons, Chichester, 2009.
[17] A. Czerwinski, J. Sobkowski, J. Electroanal. Chem. 91 (1978) 47.
[18] Z. Jusys, J. Kaiser, R.J. Behm, Phys. Chem. Chem. Phys. 3 (2001) 4650.
[19] C. Coutanceau, F. Hahn, P. Waszczuk, A. Wieckowski, C. Lamy, J.-M. Léger, Fuel Cells 2 (2002) 153.
[20] M. Heinen, Y.-X. Chen, Z. Jusys, R.J. Behm, Electrochim. Acta 53 (2007) 1279.
[21] C.M.A. Brett, A.M.F.C. Oliveira Brett, in: C.H. Bamford, R.G. Compton (Eds.), Chemical Kinetics, vol. 26, Elsevier Publ., Amsterdam-Oxford-New York-Tokyo, 1986.
[22] P. Stonehart, J. Electroanal. Chem. 15 (1967) 239.
[23] T.J. Schmidt, H.A. Gasteiger, R.J. Behm, J. Electrochem. Soc. 146 (1999) 1296–1304.
[24] M.T.M. Koper, J.J. Lukkien, N.P. Lebedeva, J.M. Feliu, R.A. van Santen, Surf. Sci. 478 (2001) L339–L344.
[25] N.M. Markovic, P.N. Ross Jr., Surf. Sci. Rept. 45 (2002) 117.
[26] K.J.J. Mayrhofer, M. Arenz, B.B. Blizanac, V. Stamenkovic, P.N. Ross, N.M. Markovic, Electrochim. Acta 50 (2005) 5144.
[27] P.S. Ruvinskiy, A. Bonnefont, M. Bayati, E.R. Savinova, Phys. Chem. Chem. Phys. 10 (2010) 15207.
[28] M. Heinen, Y.-X. Chen, Z. Jusys, R.J. Behm, Chem. Phys. Chem. 8 (2006) 2484.
[29] M. Heinen, Y.X. Chen, Z. Jusys, R.J. Behm, Electrochim. Acta 52 (2007) 5634.
[30] P. Shi, I. Fromondi, D.A. Scherson, Langmuir 22 (2006) 10389.
[31] W.E. Morf, Anal. Chim. Acta 330 (1996) 139.
[32] W.E. Morf, M. Koudelka-Hep, N.F. de Rooij, J. Electroanal. Chem. 590 (2006) 47.
[33] E.J.F. Dickinson, I. Streeter, R.G. Compton, J. Phys. Chem. B 112 (2008) 4059.
[34] D.A. King, M.G. Wells, Proc. R. Soc. London A 339 (1974) 245.
[35] Y.E. Seidel, R. Lindström, Z. Jusys, M. Gustavsson, P. Hanarp, B. Kasemo, A. Minkow, H.J. Fecht, R.J. Behm, J. Electrochem. Soc. 155 (2008) K50.
[36] Y. Takasu, T. Fujiwara, Y. Murukami, K. Sasaki, M. Oguri, T. Asaki, W. Sugimoto, J. Electrochem. Soc. 147 (2000) 4421.

[37] O.V. Cherstiouk, P.A. Simonov, V.I. Zaikowskii, E.R. Savinova, J. Electroanal. Chem. 554–555 (2003) 241.
[38] T. Biegler, D.A.J. Rand, R. Woods, J. Electroanal. Chem. 29 (1971) 269.
[39] F. Nart, W. Vielstich, in: W. Vielstich, H.A. Gasteiger, A. Lamm (Eds.), Electrocatalysis, vol. 2, Wiley, Chichester, 2003.
[40] M.R. Tarasevich, E.I. Khrushcheva, in: B.E. Conway, J.O. Bockris, R.E. White (Eds.), Modern Aspects of Electrochemistry, Plenum Press, New York, 1989 (Chapter 5).
[41] A. Lopez-Cudero, A. Cuesta, C. Gutierrez, J. Electroanal. Chem. 579 (2005) 1.
[42] G.A. Somorjai, Chem. Rev. 96 (1996) 1223.
[43] V.I. Birss, M. Chang, J. Segal, J. Electroanal. Chem. 355 (1993) 181.
[44] G. Jerkiewicz, G. Vatankhah, J. Lessard, M.P. Soriaga, Y.-S. Park, Electrochim. Acta 49 (2004) 1451.
[45] D. Zhang, O. Deutschmann, Y.E. Seidel, R.J. Behm, J. Phys. Chem. C 115 (2011) 468.